Water management in proton exchange membrane fuel cells using integrated electroosmotic pumping

Cullen R. Buie [a], Jonathan D. Posner [a,1], Tibor Fabian [a], Suk-Won Cha [a,2],
Daejoong Kim [a], Fritz B. Prinz [a,b], John K. Eaton [a], Juan G. Santiago [a,*]

[a] *Department of Mechanical Engineering, Stanford University, Stanford, CA 94305, USA*
[b] *Department of Material Science and Engineering, Stanford University, Stanford, CA 94305, USA*

Abstract

Recent experimental and numerical investigations on proton exchange membrane fuel cells (PEMFCs) emphasize water management as a critical factor in the design of robust, high efficiency systems. Although various water management strategies have been proposed, water is still typically removed by pumping air into cathode channels at flow rates significantly higher than required by fuel cell stoichiometry. Such methods are thermodynamically unfavorable and constrain cathode flow channel design. We have developed proton exchange membrane fuel cells (PEMFCs) with integrated planar electroosmotic (EO) pumping structures that actively remove liquid water from cathode flow channels. EO pumps can relieve cathode design barriers and facilitate efficient water management in fuel cells. EO pumps have no moving parts, scale appropriately with fuel cells, operate across a wide range of conditions, and consume a small fraction of fuel cell power. We demonstrate and quantify the efficacy of EO water pumping using controlled experiments in a single channel cathode flow structure. Our results show that, under certain operating conditions, removing water from the cathode using integrated EO pumping structures improves fuel cell performance and stability. The application of EO pumps for liquid water removal from PEMFC cathodes extends their operational range and reduces air flow rates.
© 2006 Elsevier B.V. All rights reserved.

Keywords: Proton exchange membrane; Fuel cell; Electroosmotic pump; Water management

1. Introduction

Proton exchange membrane fuel cells (PEMFCs) are being developed for electric power generation for portable hand-held electronics [1–3] as well as emission-free energy sources for automobiles and secondary power generation [4–8]. Numerous recent experimental and numerical studies conclude that water management in PEMFCs is critical to reliable and efficient operation [5–24]. The majority of PEMFCs use polyperfluorosulfonic acid membranes; e.g., Nafion® membranes manufactured by DuPont, as the electrolyte. Ion transport occurs along pathways established by anionic (sulfonic acid anion) groups within the hydrated polymer. The ionic conductivity of typical electrolyte membranes is therefore dependent upon proper hydration levels [17,25]. Several mass transport and reaction mechanisms affect PEM hydration including diffusion, electroosmotic drag, and evaporation and condensation in reactant gas streams [15,17,19,23,25]. Maintaining adequate hydration is difficult as such mechanisms are strongly coupled and, in most cases, not easily predicted. At low current densities, the cell produces little water and water removal from the cell is relatively easy. At high current densities, more water is produced and electroosmotic drag of water to the cathode can dry the anode and flood the cathode. This phenomenon complicates the overall hydration mechanism of the electrolyte membrane.

Cathode flooding occurs when water production at the oxygen reduction reaction and electroosmotic drag of water to the cathode exceed the water removal rate resulting from air based advection, evaporation, and back diffusion. Liquid water that builds up at a fuel cell cathode decreases performance and

---

* Corresponding author at: Building 530, Rm. 225, 440 Escondido Road, Stanford, CA 94305, USA. Tel.:+1 650 723 5689; fax: +1 650 723 7657.

E-mail address: juan.santiago@stanford.edu (J.G. Santiago).

[1] Present address: Department of Mechanical & Aerospace Engineering, Arizona State University, Tempe, AZ 85287, USA.

[2] Present address: School of Mechanical & Aerospace Engineering, Seoul National University, Seoul, Korea.

Nomenclature

a	pore radius
A_{eo}	pump cross sectional area
A_{FC}	fuel cell active area
F	Faraday constant
I''_{eo}	EO pump current density
j	fuel cell current density
L	pump thickness
M	molecular weight
p_{air}	air pressure
Δp	pressure drop
P''_{eo}	power consumed by EO pump (per unit area)
P''_{FC}	fuel cell power density
Q	flowrate
R_A	resistance between electrode and EO pump
R_u	universal gas constant
t	time
T	temperature
V_{FC}	fuel cell voltage
V_{eff}	effective potential drop across pump
V_{app}	applied potential drop across pump
V_{dec}	decomposition potential
V_{FC}^{on}	fuel cell voltage with the EO pump on
V_{FC}^{off}	fuel cell voltage with the EO pump off
Z	impedance

Greek

α	ratio of actual air flow rate to stoichiometric flow rate
χ	normalized fuel cell performance increase
κ	permeability of porous media
λ_D	Debye length
μ	dynamic viscosity
ρ	density
σ_∞	bulk electrolyte conductivity
τ	tortuosity
Ψ	porosity
ζ	zeta potential

inhibits robust operation [9–11,21,23,26–28]. Flooding in the cathode reduces oxygen transport to reaction sites and decreases the effective catalyst area [9–11,23]. Cathode flooding can result in a catastrophic decrease of performance and has been observed over a wide range of operating conditions. Recent work has shown that cathode flooding can be predicted [9,26,29], detected experimentally [16,27,30], and depends on local current density [31], operating temperature, GDL properties (e.g., porosity and hydrophobicity), air flow rate and relative humidity, and fuel cell design.

Perhaps the most critical aspect of fuel cell water management is the delicate balance between membrane hydration (favoring high water content) and avoiding cathode flooding. Over the last 15 years several different methods of water management have been proposed. Humidification of the reactant gases is typically employed to eliminate membrane dry out [7,18,19,32,33] but humidification alone does not address cathode flooding. One method of removing liquid water is to employ long, serpentine oxidant channels where the hydraulic resistance of liquid water is in series with gas transport, and so gas streams drive out excess liquid water [9,34]. In such designs, the fraction of water content along the channel length increases steadily in the direction of the outlet. A second method of cathode flooding control is known as anode water removal, where water is forced through the permeable PEM using strong cathode-to-anode pressure differentials [5,8,35]. Cathode streams are operated at significantly higher pressures than the anode stream and gas velocity in the anode channels is increased. This method is effective but requires relatively high pressures (3–5 atm) and flow rates which draw considerable parasitic power. A third and very common flooding mitigation strategy is simply increasing cathode gas flow rate in order to remove liquid water via evaporation and advection [5,9,11,36]. Effective operation is typically achieved by increasing operating air flow rate well above stoichiometric levels [11] or periodically flushing the cathode with momentarily high air flow rates [34,36]. In the former, operational air flow rates are often 2–60 times the rates required by stoichiometry and therefore energetically unfavourable [11,36]. In the latter, valving structures and control schemes are employed which add system complexity and may require integrated water detection.

A few proposed water management schemes have involved integration of additional or replacement materials into the membrane electrode assembly (MEA) and/or electrodes. A common form of water management involves optimization of the gas diffusion layer (GDL). Ideally, the GDL allows reactant gases access to the reaction zones without inhibitng outflow of gaseous reaction products. GDL is enlisted in water management by the integration of polytetrafluoroethylene (PTFE), so that water is rejected via hydrophobic surface forces [28,37–42]. Another water management technique involves the incorporation of a hydrophobic microporous layer between the GDL and catalyst to prevent liquid water blockage of reaction zones. Microporous layers are commonly employed and several studies have been conducted to elucidate their benefits [43–47]. In an effort to alter electrolyte properties, Watanabe et al. proposed polyperflourosulfonic membranes with self-humidifying characteristics [20]. These use H_2 and O_2 crossover and have integrated platinum electrocatalysts and hygroscopic particles to produce and store water inside the electrolyte. They found recombination of crossover H_2 and O_2 was sufficient to hydrate 50 μm thick membranes using minimal external humidification. Lastly, PEMFCs have been proposed that incorporate special hydrophilic wicking structures into cathode flow channels to redistribute liquid water [12,22,48]. UTC Fuel Cells has developed an innovative water management technique using porous bipolar plates [49]. This passive water management method relies on hydraulic permeation and capillary action to drive liquid water from flooded regions of the cathode to dryer regions or out of the stack.

In this work we propose a new water management technique whereby liquid water in hydrogen-air fuel cell cathodes is

actively pumped out of the fuel cell using an integrated porous electroosmotic (EO) pumping layer. EO pumps are compact, have no moving parts, and scale favorably with fuel cell design. We show that integrated EO pumps effectively remove liquid water from the cathode, enabling air flow rates of just two to three times stoichiometric requirements. Additionally we show that this active pumping method consumes a small fraction of the fuel cell power.

2. Theory

In this section we summarize a simple model for the prediction of flow rate, pressure, current, and power consumption of electroosmotic pumps as a function of the pump geometry and working electrolyte. We then present a model for estimating the minimum theoretical fraction of fuel cell power consumed by an EO pump integrated with a PEMFC.

2.1. Porous electroosmotic pumps

Electroosmosis uses ion drag in micro- and nano-scale flow channels to advect electrolytes [50]. It has been applied for sample control in electrokinetic devices for chemical analysis [51] and stand-alone pumps that serve as flow rate and pressure sources. Yao and Santiago [52] review electroosmotic pumps including theory, designs, and applications. Laser and Santiago [53] present a review of miniature pumps in which electroosmotic pumps are discussed. EO pumps have no moving parts and require structures with high surface-to-volume ratio. They have been fabricated using glass-particle-packed fused silica capillaries [54,55], porous borosilicate glass [56], in situ polymerized porous monoliths [57], and porous silicon [58]. They have also been bulk micromachined in soda-lime glass [59] and silicon substrates [53]. The technology offers the ability to achieve high pressures (more than 340 atm at 12 kV applied potentials [55]) and high flow rate in a compact form (e.g., 40 ml min^{-1} at 100 V in a pumping structure less than 1 cm^3 in volume) [56,58]. For integration with PEMFCs, we use porous borosilicate glass structures available commercially and fabricated by sintering of glass particles [56].

Electroosmotic flow is the motion of an electrolyte caused by the interaction of an external electric field with the diffuse charges of electrical double layers (EDLs), which form at electrolyte/surface interfaces [50]. In glass substrates, EDLs result from spontaneous deprotonation of surface silanol groups upon contact with water. Porous glass EO pumps offer large surface-to-volume ratio and relatively high zeta potential, ζ defined as the potential drop associated with the diffuse charges of the EDL. We model EO flow in porous structures as through many torturous channels acting in parallel as shown in Fig. 1. Depicted here is a velocity profile in the absence of a significant pressure gradient.

The EDL contains a region of excess of positive ions that shield the negative surface charge. The EDL's characteristic thickness is the Debye length λ_D [50]. The externally applied field acts on mobile charges in the EDL and generates bulk flow. The flow rate, Q, of a porous EO pump can be
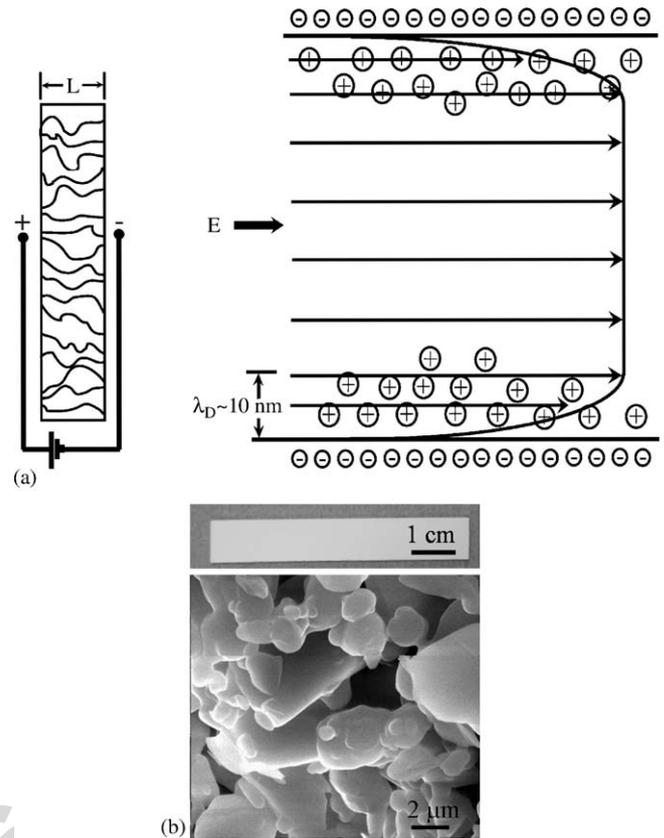
Fig. 1. A porous glass electroosmotic pumping structure. (a) Schematic of porous glass medium modeled as many cylindrical microchannels in parallel. The pumping structure is characterized by cross sectional area A, porosity φ and tortuosity τ. A small section of a single channel within the porous material is depicted on the right. An EDL spontaneously forms on the glass/electrolyte interface. Bulk motion in the channel is generated by a coupling of the applied electric field E and the mobile region of net charge in the EDL. (b) Image of a 1 cm × 6 cm porous glass frit used in this study (top) and a scanning electron micrograph of porous structure showing order 1 μm pores (bottom).

expressed as,

$$Q = \frac{\psi}{\tau} \left[-\frac{\Delta p A_{\text{eo}} a^2}{8 \mu L} - \frac{\varepsilon \zeta A_{\text{eo}} V_{\text{eff}}}{\mu L} f \right], \tag{1}$$

where Ψ is porosity, τ is tortuosity, L is pump thickness, A_{eo} is (macroscopic) cross-sectional area of the pumping media, a is pore diameter, Δp is pressure drop across the pump, μ is dynamic viscosity of the fluid, and ε is permittivity of the fluid. ζ depends on the surface chemistry and electrolyte properties such as ion concentration and pH. f takes into account the effects of finite EDLs and is determined from numerical solutions to the nonlinear Poisson–Boltzmann equation governing electric potential in the EDL[52]. V_{eff} is the effective potential drop across the pump substrate and can be approximated as,

$$V_{\text{eff}} = V_{\text{app}} - V_{\text{dec}} - 2R_A I_{\text{eo}}. \tag{2}$$

Here V_{app} is the applied potential, V_{dec} is the decomposition potential (including theoretical electrode potentials and overpotential) associated with Faradaic electrode reactions, R_A is the electrode-to-pump structure electric resistance, and I_{eo} is the EO pump current. Maximum pump flow rate and pressure can

Table 1
Typical electoosmotic pump parameters

Parameter	Value
A	12 cm^2
L	1.1 mm
ζ	−48 mV
σ_∞	170 μS cm^{-1}
a	1 μm
Ψ	0.45
τ	1.45
V_{app}	14 V
V_{eff}	5.0 V
f	0.98
g	0.80

be derived from Eq. (1) by setting pressure and flow rate equal to zero, respectively.

The total current of an electroosmotic pump is the sum of ionic advection and electromigration within the pump. The maximum current density of a porous EO pump is given as,

$$I''_{eo} = \frac{\psi \sigma_\infty}{\tau} \frac{V_{eff}}{L} \frac{f}{g}, \tag{3}$$

where g is a function of the ion distribution in the EDL [52]. The maximum power density consumed by the EO pump can be expressed as $P''_{eo} = V_{app} I''_{eo}$. Typical parameters for porous glass EO pumps are given in Table 1. The values given here for ζ, f, and g are consistent with deionized water exposed to the atmosphere at 25 °C [54]. Note that water exposed to the atmosphere quickly becomes saturated with carbon dioxide from the air, and dissolved carbon dioxide reacts with water to create carbonic acid, which lowers pH and increases conductivity. In the next section, we present simple relations for fuel cell water production and we estimate the minimum theoretical fraction of fuel cell power that is consumed by an EO pump.

2.2. Parasitic power model

The stoichiometric volume flow rate of air required by a fuel cell can be related simply to fuel cell current density j as,

$$Q_{air,stoich} = \frac{R_u T}{4F} \frac{j A_{FC}}{p_{air} s}, \tag{4}$$

where R_u is the universal gas constant, F is Faraday's constant, s is the volume fraction of oxygen in air, p_{air} is channel air pressure, A_{FC} is the fuel cell area, and T is local cell temperature. We define $\alpha = Q_{air}/Q_{air,stoich}$ as the ratio of air flow rate delivered to the cell to the air flow rate required by stoichiometry. The maximum amount of liquid water produced by the fuel cell can be expressed as,

$$Q_w = \frac{j A_{FC} M_w}{2 F \rho_w}, \tag{5}$$

where ρ_w and M_w are the density and molecular weight of liquid water, respectively. The power output of the fuel cell is the product of the cell potential and the current produced, and can be expressed as $P''_{fc} = V_{fc} j$. Here V_{fc} is fuel cell voltage, a function

of the current density and activation, ohmic, and mass transport losses. For a complete description of the cell performance and losses see Bernardi and Verbrugge [8]. Combining Eqs. (1) and (5) we estimate the theoretical minimum effective pump voltage required to remove water produced by the fuel cell,

$$V_{eff} = -\frac{\Delta p a^2}{8 \varepsilon \zeta f} - \frac{\tau \mu A_{FC} j L M_w}{2 \psi \varepsilon \zeta \rho_w A_{eo} F f}, \tag{6}$$

which can be combined with Eqs. (2) and (3) to estimate the minimum theoretical power consumed by the EO pump,

$$\frac{P_{eo}}{P_{FC}} = \left(\frac{\psi f}{\tau g} \frac{\sigma_\infty V_{eff}}{L j} \right) \left(\frac{V_{eff} A_{eo}}{V_{FC} A_{fc}} \right)$$
$$\times \left[1 + \frac{2 R_A \psi \sigma_\infty f A_{eo}}{\tau L g} + \frac{V_{dec}}{V_{eff}} \right]. \tag{7}$$

Eq. (7) assumes that the pump only removes water produced by the fuel cell (e.g., assumes no water is introduced via humidified gas streams) and neglects electroosmotic drag from the anode to the cathode. Further, Eq. (7) assumes water is pumped uniformly over the pump area, at a steady rate, and across a pressure difference Δp. The formulation suggests P_{eo}/P_{FC} depends strongly on the effective EO pump voltage. As expected, higher fuel cell power, $V_{FC} j A_{fc}$, requires higher pump power. The decomposition voltage, V_{dec}, is typically between 2 and 4 V; A_{eo}/A_{FC} should be significantly less than one in many designs; Ψ/τ for porous structures is typically between 0.14 and 0.31; and minimum L values are typically limited by fabrication and structural strength limitations. Electrode-to-pump resistance, R_A, should be minimized (we estimate a total of 50 Ω in our design). f and g are determined by the selection of pump pore diameter. Minimum pore size is dictated either by availability of materials or, as in our case, a tradeoff between achieving enough pressure, Δp, while achieving fast, robust removal of water. As we shall discuss in a latter section, the conductivity of water produced by our fuel cell, σ_∞, typically has values of about 170 μS cm^{-1} or greater due to impurities absorbed from contact with fuel cell materials and carbonic acid ions from CO_2 absorption.

Eq. (7) is useful in placing a minimum on the order of magnitude of the theoretical power required by the EO pump, and assessing the basic feasibility of the concept. However, care should be taken in applying Eq. (7) to predict accurate design performance. For example, our experiments suggest that only a fraction of an integrated EO pump is active at any one time, as water is generated non-uniformly within fuel cell cathode. Also, sections of the EO pump, which are wet but exposed to gas on both sides can consume power while not resulting in appreciable pumping. (We have confirmed this "power without flow rate" operation in independent experiments with wet porous glass/electrode assemblies which are exposed to air on both sides; and we attribute the lack of pumping in such experiments to the finite capillary pressure that must be exceeded for the pump to "dry" itself via electroosmosis.) We therefore advocate that Eq. (7) be used to predict pump performance not using the minimum voltage predicted by Eq. (6) but using Eq. (2) with a V_{app} derived from empirical observations of effective water removal in similar structures.

As an arbitrary example, consider a 1 cm^2 fuel cell that can generate 1 A at 0.5 V with a net power output of 500 mW. Using Eq. (5), we estimate that the fuel cell will generate a maximum of about 5.6 μL min^{-1} of liquid water. A simple application of Eqs. (6) and (7) suggests an absolute minimum EO pump power of 19.2 mW or 3.8% of the PEMFC power. However, as discussed above, we find Eq. (6) under predicts pump voltage required for effective water removal. From our experimental observations in several designs, we have found V_{app} values of order 14 V are required (versus the theoretical minimum V_{eff} of 4.1 V). For these conditions, Eqs. (2) and (3) suggest that the parasitic pump power will be about 13% of fuel cell power. Table 1 summarizes the critical parameters used in the above calculations. As we shall discuss in a latter section, this is in agreement with exper-imentally observed trends.

3. Experimental set-up and methodology

In this section we present the design of a fuel cell integrated with EO pumping structures and our system-level experimental set-up.

3.1. PEMFC with integrated EO pump design

We used a linear, single channel fuel cell to more effectively control experimental parameters and quantitatively describe the effect of flooding as a function of current density. This single channel design also simplifies the integration of the EO pump. Prior fuel cell studies focusing on cathode channel flooding have been performed using similar designs [11,31,60]. A diagram of the fuel cell design is shown in Fig. 2. The anode current collec-tor is a 1 mm thick 316 stainless steel plate with a 2 mm wide, 60 mm long slot that serves as the hydrogen gas flow channel. The channel is machined using a wire electrical discharge pro-cess (EDM-Tek, Union City, CA) and then electroplated with a 1 μm thick gold layer to inhibit electrochemical degradation and reduce contact resistance. The membrane electrode assembly (MEA) (BCS Fuel Cells Inc. Bryan, TX) comprises a Nafion 112 membrane with 350 μm thick carbon cloth gas diffusion layers (GDLs) and a 1 mg cm^{-2} platinum catalyst loading. (The GDL is 6 mm wide by 66 mm in length.) Two 1.1 mm thick porous glass EO pumps, spaced 2 mm apart, make up the walls of the cathode channel. The resulting cathode channel is 2 mm wide, 60 mm long, and 1.1 mm high. We roughly estimate the effective
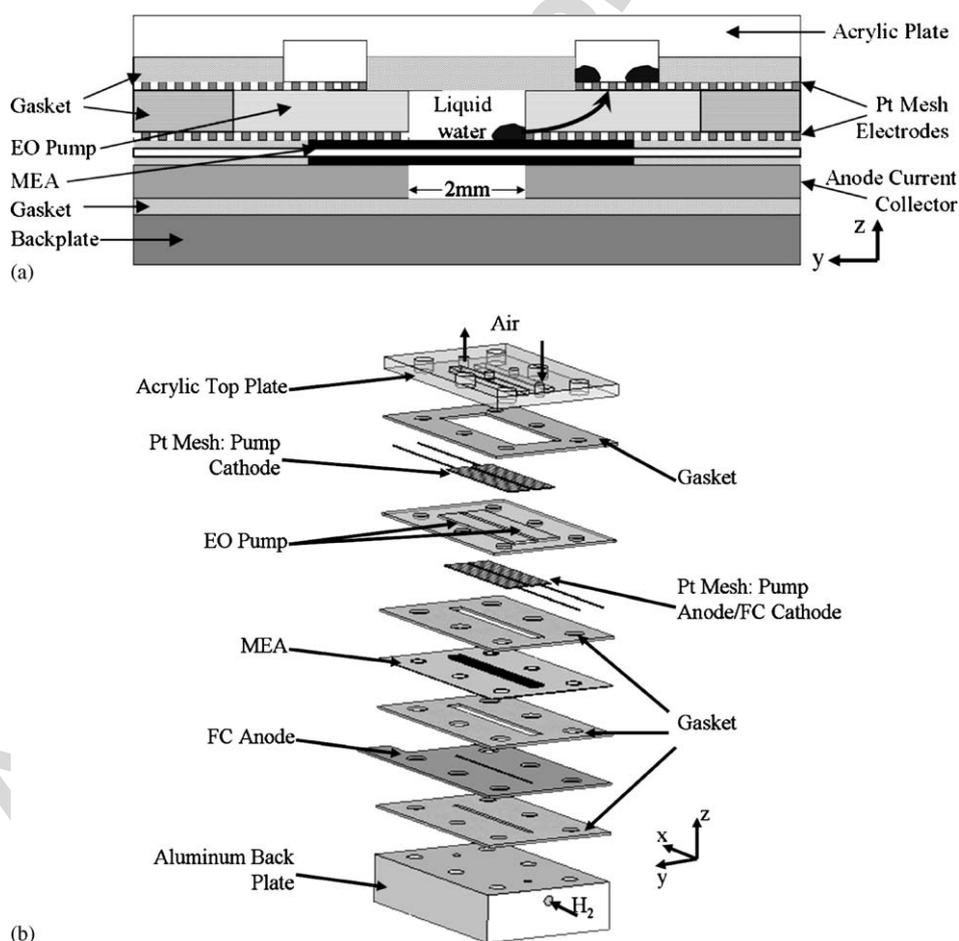

Fig. 2. Schematic of the cross-sectional area (a) and exploded view (b) of our PEMFC design showing integrated electroosmotic pumping structures. In (a) hydrogen and air flow are into the page. Water formed due to oxygen reduction reaction at the cathode is forced out of the GDL via hydrophobic forces where it coalesces into droplets. Liquid water droplets are wicked into the hydrophilic porous glass structure of the EO pump. Once the EO pump structure is adequately saturated with water, EO pumping actively drives water through the porous glass structure and into integrated water reservoirs in the acrylic top plate.

pumping area and pump length of this design as the edge area of the pump (1.1 by 60 mm) and the diagonal length between the channel and the water chamber at the top level (∼7 mm).

A pure platinum (Pt) mesh (Goodfellow Cambridge Limited, UK) (0.06 mm diameter wires on a square grid with center-to-center spacing of 0.25 mm) serves both as a fuel cell cathode and an EO pump anode, so that these two electrodes share a common potential. We use this mesh because preliminary experiments have shown that pump potentials (4–20 V) corrode thin gold coatings on stainless steel originally used for the fuel cell cathode. Further evaluation of the material for the fuel cell cathode/EO pump anode electrode is a good area for future study. For example, we observe that gold coated 316 stainless is not suitable as an EO pump anode, as it undergoes an oxidation reaction that fouls the EO pumping structure (perhaps forming mobile Au^{2+} ions that then adsorb to EO pump pores). We are currently evaluating less expensive substrates, such as graphite or steel with a sputtered or electroplated platinum coating.

Two 10 mm wide and 60 mm long porous glass frits (Robu-Glas, Germany) are potted (i.e., with epoxy) into a laser machined, 1 mm thick acrylic plate and placed directly on the fuel cell cathode/EO pump anode. Another Pt mesh serves as the EO pump cathode. The final layer of the fuel cell is a laser machined acrylic top plate with recessed channels for water removal. Each layer of the fuel cell is sealed with 350 μm thick silicon rubber gaskets as shown in the exploded view of the device in Fig. 2b. The fuel cell's multi-layer design allows for fast assembly, repeatable performance across assemblies, and ease of disassembly (e.g., to visually inspect channels for flooding).

The operation of the EO pump structure is as follows. When the EO pump is dry, its low permeability results in negligible leakage of air. Upon activation of the fuel cell, water which first forms in the fuel cell cathode channel wicks into the hydrophilic porous pump substrate until saturation. In this way, the pump is initially a passive water management device that prevents cathode flooding via capillary action. After about 60 min of operation at typical conditions, the pump is largely saturated with water

and the EO pump electrolytic circuit is completed. At this point, the potential applied to the EO pump causes water to be pumped out of the cathode air channels (from EO pump anode) and into the acrylic top plate water reservoirs (to and through EO pump cathode). The water can be collected here or purged from the device (e.g., passively by evaporation or dripping water out of the system).

3.2. Experimental set-up

For all of our experiments (with the exception of the electrochemical impedance spectroscopy measurements), the set-up consists of a fuel cell, a boost power supply (Acopian W3.3MT65, Easton, PA) set at 3.3 V, and an electronic load (Agilent N3100A). These and other components are shown in the schematic of Fig. 3. The power supply is connected in series with the fuel cell to supplement the voltage provided by the electronic load. The load is operated in a four-wire mode with the source wires connected to the series combination of the fuel cell and the boost power supply, and the sense wires connected to the fuel cell. The air and hydrogen flow rates are controlled using two mass flow controllers (Alicat Scientific, Tucson, AZ) calibrated for air and hydrogen, respectively. The setting of the active load properties (including cell potential) and mass flow levels are automated using a PC running LabView, a GPIB card, and an IO data acquisition card (National Instruments, Austin, TX). The EO pump electrical potential is supplied by a DC power supply (Agilent 6030A DC Electronic Load, Palo Alto, CA). Dry air and hydrogen are supplied to the system from compressed gas cylinders regulated at 15 kPa. The gases exiting the flow controllers are humidified using a custom water-bath sparging unit at 60 °C. After leaving the sparging unit, the gases are cooled as they flow through a 0.5 m long teflon tube and are delivered to the cell at room temperature and 100% RH. Table 2 summarizes the essential parameters used in all of the experiments. For the electrochemical impedance spectroscopy (EIS) experiment, we used a Solartron (Shildon, UK) 1287A Potentiostat and 1260A Impedance/Gain-Phase Analyzer in place of the electronic load and boost power supply.
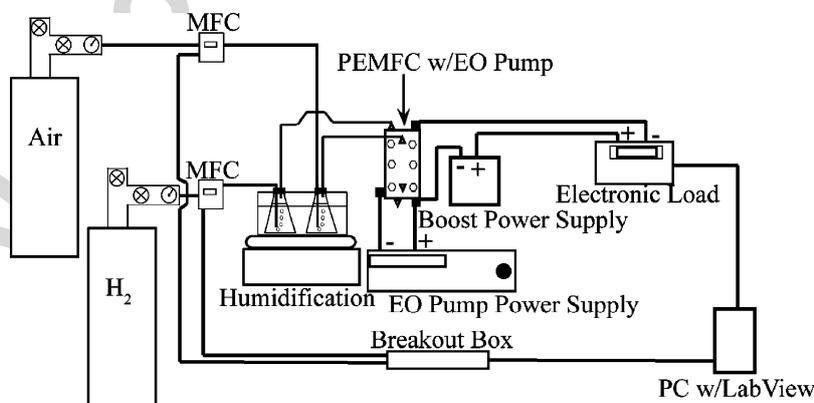

Fig. 3. Schematic of the experimental set-up. Hydrogen and air are supplied to the system via compressed air cylinders and flow rates are regulated with two mass flow controllers (MFCs) (Alicat Scientific, Tucson, AZ). In all experiments, the gases are delivered to the fuel cell at 100% RH. The flow rate of hydrogen and air and the Agilent electronic load are set automatically using a PC running LabView software. The power supply is operated manually and used to apply the driving potential for the EO pump.

Table 2
Experimental parameters

Parameter	Value
Fuel cell electrolyte	Nafion 112
Gas diffusion layer	350 μm E-Tek anode and cathode
Active area	1.2 cm^2
Anode and cathode channel dimensions	2 mm × 60 mm × 1.1 mm ($W \times L \times H$)
Catalyst loading	1 mg cm^{-2} Pt, anode and cathode
Anode gas	H$_2$ (>99.995%)
Anode gas temperature/humidity	23 °C, 100% RH
Anode flow rate	Stoichiometric equivalent for 4 A cm^{-2}
Cathode gas	Air (79% N$_2$, 21% O$_2$)
Cathode gas temperature/humidity	23 °C, 100% RH
Cathode flow rate	Stoichiometry dependent
Fuel cell temperature	23–26 °C
Electroosmotic pump voltage	14 V

4. Results

In this section we show that removing water from PEMFCs using electroosmotic pumps can enhance fuel cell performance and prevent cathode flooding using minimal parasitic power loads. We have conducted extensive preliminary testing to verify that our single channel fuel cell floods across a wide range of operating conditions. This preliminary work included variations of current density and fuel cell potential, temperature of incoming gas streams, and relative humidity of incoming streams. As expected, the steady state voltage of the cell depends on the current density and the air flow rate ratio, α. We can summarize much of these preliminary observations of cathode flooding by simply noting that (with the EO pump inactive) our cathode flooded routinely within about 20 min of running 1 A cm^{-2} current densities or greater. The next few sections describe the effects of flooding quantitatively as a function of current density and excess air flow rate ratio α. Most importantly, we will compare the cases of inactive and active EO pump to demonstrate the effectiveness of our water management method. The EO pumps were able to prevent flooding across the full range of conditions explored, and accomplished this with minimal parasitic power consumption.

By initiating our experiments from a flooded condition we are able to quantify the relative benefit of a PEMFC with an active EO pump versus the system with an inactive EO pump. In the following sections we explore first the transient cell potential at constant current density (galvanostatic) and then the steady state cell performance over a range of current densities and stoichiometric air flow rates (in a series of cell polarization data).

4.1. Galvanostatic measurements

We first present anecdotal results demonstrating the transient performance of the EO pump water management strategy. Specifically, we present time histories of galvanostatic fuel cell measurements under flooding conditions with and without EO pumping.

The initial condition of these and all of the experiments presented in this paper are as follows. In all cases, we first purged
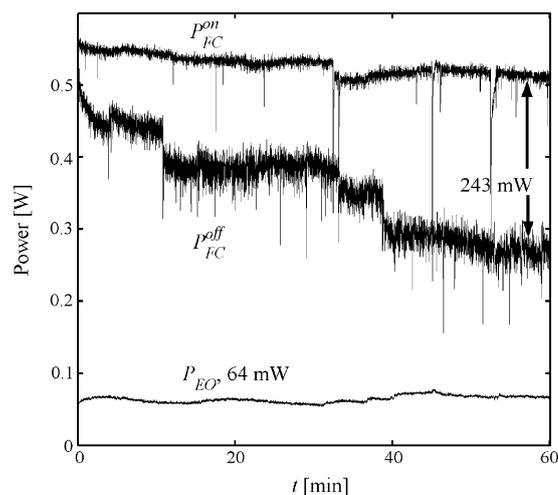

Fig. 4. Galvanostatic measurements of fuel cell potential with EO pump active (top trace) and inactive (middle trace). Pump power is approximately 64 mW (bottom trace). This experiment is performed at a current density of 0.83 A cm^{-2} and $\alpha = 3$. The experiment is initiated with a dry MEA. Without activation of the EO pump, the cell power degrades to 0.27 W over about 60 min; a deterioration of performance attributed to GDL flooding. Activation of the EO pump prevents this flooding and maintains a steady state value of about 0.51 W. After 1 h of run time, the EO pump results in a gross fuel cell output 243 mW higher (a net system power increase of 179 mW).

the anode and cathode channels by running dry air through both channels for 15 min. We then switched to humidified air and hydrogen streams, and initiated the fuel cell active load. After a measured interval of time (to be reported with each data set below), we then activated the EO pump. This process ensured repeatable hydration conditions of both the MEA and EO pump structure at the start of each experiment.

Fig. 4 shows a representative galvanostatic experiment at $\alpha = 3$ and current density of 0.83 A cm^{-2} with and without (immediate) activation of the EO pump. (The state of the EO pump is indicated by the superscripts "on" and "off", while subscripts are reserved as descriptors of the fuel cell). Also shown in the figure are measurements of the instantaneous power consumed by the EO pump (active EO pump operation). The fuel cell power drops from 0.5 W to less than 0.3 W within about 1 h of continuous operation with the EO pump inactive (bottom power trace) and the operation is characterized by large, unsteady fluctuations in fuel cell power (and current). We attribute this decrease in power and relatively large fluctuations directly to cathode flooding [11,12,14,61,62]. This and other conclusions regarding flooding presented here are substantiated by the preliminary experiments including observations of liquid water exiting flooded cathodes and direct observation of liquid water upon disassembly of the device. For the activated EO pump case, the cell power only slightly decreases until reaching a long-term value of 0.51 W after 30 min. In the inactive EO pump experiment, the cathode produces more water than can be removed by evaporation and advection, resulting in flooding. For the activated EO pump case, excess liquid water formed at the cathode is removed and observably pumped into the water reservoirs at the top layer of the device.
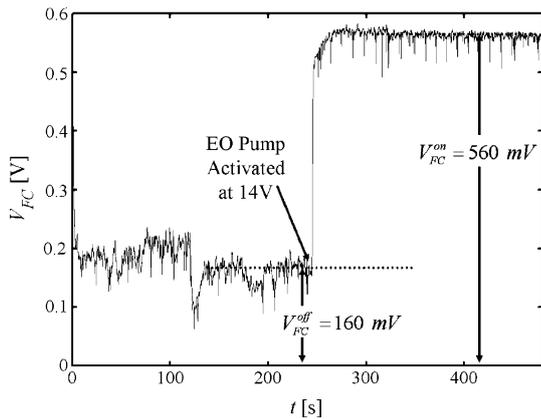
Fig. 5. Galvanostatic (constant current) measurement versus time. This experiment was conducted after the fuel cell was operated with a deactivated EO pump for 1 h at a constant current density of 1 A cm^{-2} in order to flood the GDL. For the first 240 s, the partially flooded fuel cell is run with a deactivated EO pump. The pump is activated at 240 s and the fuel cell voltage quickly (within about 15 s) increases to 560 mV. This result is typical of the performance increases enabled by the EO pump. Activation of the EO pump clearly benefits the flooded fuel cell, increasing average fuel cell voltage by 390 mV in this case.

Fig. 4 also shows that the EO pump draws minimal power while substantially increasing net system power output. We found that a steady pump potential of 14 V was sufficient to rapidly remove water and prevent flooding across all conditions explored, and so chose this value for all experiments. In this case the pump potential results in a 4.5 mA current and a pump power consumption of about 64 mW. Comparing the two cases, after 1 h of operation at 0.83 A cm^{-2}, the activated EO pump yields a 66% net increase in the power output of the system (from 270 mW net output to about 450 mW net output). The EO pump also greatly decreases fuel cell voltage fluctuations, suggesting a more stable operation is achieved using EO pumping. For example, the standard deviation of the fuel cell power after 1 h of operation with the EO pump active is 6 mW, compared to a value of 15 mW for the inactive EO pump case. For inactive EO pump operation, we observed intermittent ejections of water droplets from the air stream outlet, and so we attribute these high power fluctuations to the effects of partial cathode flooding.

Fig. 5 shows the fuel cell potential following 1 h of operation with the EO pump inactive ($t = 0$ is after 1 h of operation) at $\alpha = 3$ and $j = 1$ A cm^{-2}. The figure defines V_{FC}^{on} as the fuel cell potential for an activated EO pump run and V_{FC}^{off} as cell potential with EO pump deactivated (this notation will be used throughout the paper). At the start of this experiment, the fuel cell is flooded and shows a potential of 0.2 V. After an additional run time of 4 min, the EO pump is activated ($t = 240$ s) and the fuel cell potential increases from 160 to 560 mV in less than 15 s. In this case, activation of the pump results in a 220% net increase in the power output of the fuel cell. Together, Figs. 4 and 5 indicate that the EO pump can be used both to prevent flooding (Fig. 4) and to remove water from a fuel cell that is flooded (Fig. 5).

4.2. Polarization and power density curves

In this section we present characterization of the fuel cell potential as a function of current density, j, and stoichiometric
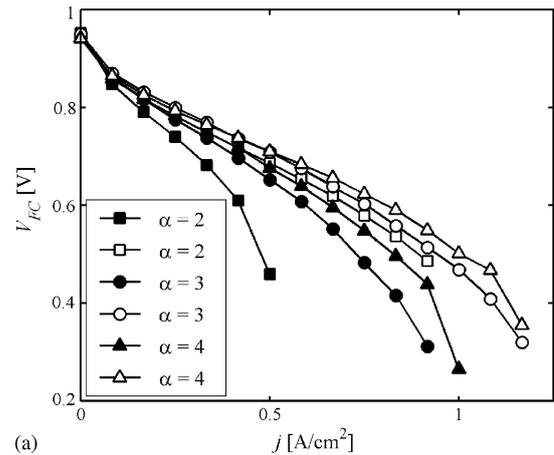

(a)
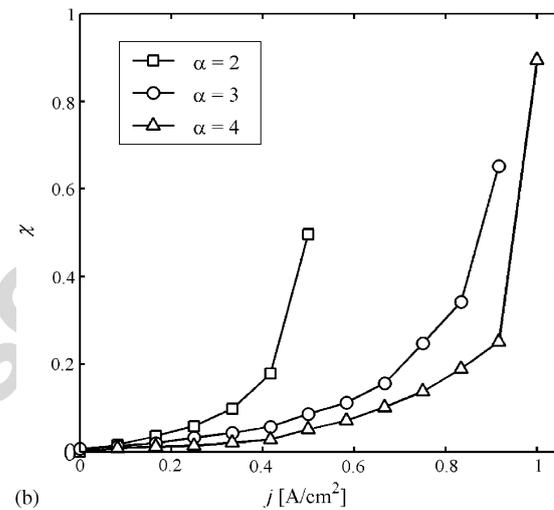
(b)

Fig. 6. Polarization curves (a) with $\alpha = 2$–4 without activation of EO pump (closed symbols) and with activation of EO pump (open symbols) at $V_{app} = 14$ V. In all cases the fuel cell is operated at 1 A cm^{-2} for 1 h prior to obtaining these polarization measurements. The data shows that fuel cell performance increases with α, as expected, and with the activation of the EO pump. (b) Shows that the nondimensional performance increase factor, χ, increases for higher current density and lower values of α.

air flow ratio, α, with and without EO pump activation. Prior to each polarization data series, the fuel cell is purged with dry air for 15 min and subsequently operated with the EO pump deactivated for 60 min at 1 A cm^{-2}. This process is conducted to ensure repeatable membrane hydration. Fig. 6a shows polarization curves at stoichiometric air flow ratios of 2–4 with and without EO pump activation. Open symbols indicate an activated EO pump and closed symbols a deactivated pump. The data acquisition system was programmed to first obtain data at low current densities, and then for increasing current densities until the fuel cell instantaneous output voltage fell below 0 V (indicating either flooding or overly inefficient operation at high current density). Below 0.83 A cm^{-2}, measurements were obtained after 2 min of operation at each new current density; and above 0.83 A cm^{-2}, measurements were obtained after 5 min of operation. Independent experiments showed this larger time at high current density ensured near steady operation in the cell's mass-transfer-limited regime. The polarization curves exhibit

behavior typical of PEMFCs with three distinct loss regions, namely activation, ohmic, and mass transport [63]. The data also shows that cell performance increases with increasing stoichiometric ratio α, as expected [21,64]. For each α, the cell potential is significantly increased with EO pump operation. The rise in cell potential increases with cell current density because conditions most conducive to flooding benefit most from EO pump operation. We summarize the benefit of EO pumping in Fig. 6b. Here we plot a normalized fuel cell potential difference χ, defined as

$$\chi = \left(\frac{V_{FC}^{on} - V_{FC}^{off}}{V_{FC}^{off}} \right), \tag{8}$$

as a function of fuel cell current density, j. Note V_{FC}^{on} and V_{FC}^{off} correspond to open and closed symbols shown in Fig. 6a, respectively. The normalized fuel cell potential difference, χ, increases with increasing current density for all stoichiometric ratios α. This again supports our conclusion that EO pumps increase fuel cell performance by preventing flooding as more water is produced at higher current densities. Further, the slopes and absolute value of χ both increase with decreasing α since water removal via air stream advection is least effective at low α.

Note that activation of the EO pump is beneficial even at low current densities (e.g., χ is already 0.06 at $j = 0.25\,\mathrm{A\,cm^{-2}}$ for $\alpha = 2$). Flooding is generally attributed to operation at high current densities but several studies have indicated that water management is an issue in all operating regimes [9,23,26]. The present polarization curves show that the EO pump structure improves PEMFC performance even at low current densities where the cell produces a small amount of liquid water. The EO pump, of course, provides the most benefit at conditions that favor flooding, high j and low α.

Next we present measurements of gross (fuel cell output discounting pump) and net (fuel cell output minus pump input) power for the fuel cell. Fig. 7a–c respectively are power density curves for $\alpha = 2$–4 obtained from the polarization data of Fig. 6a. In each case the voltage applied to the EO pump is 14 V and the power consumed by the pump is approximately uniform at 56 mW. (This is slightly lower than the 64 mW reported in an earlier section due to conductivity variations discussed in the following section). Fig. 7a shows that activation of the EO pump is most beneficial for the $\alpha = 2$ case, as expected. Here, the net power output of the PEMFC/EO pump system increases by 57% and the maximum current density of the cell increase by about a factor of 2 when the EO pump is activated. Fig. 7b shows power density curves at $\alpha = 3$, for which there is an intermediate benefit due to EO pumping. Here, the EO pump increases net maximum power output of the cell by 18% (gross maximum fuel cell power output is increased by 28%). Fig. 7c shows measurements for $\alpha = 4$, where net maximum power output is increased by 13% (gross maximum power increased by 22%). Lastly, note how the data obtained with an active EO pump (open symbols) extends to higher current densities; showing how EO pumping extends operation of the fuel cell to current density values inaccessible to the fuel cell without EO pumping. Collectively, the data of Fig. 7 illustrate EO pumping significantly increases the net fuel
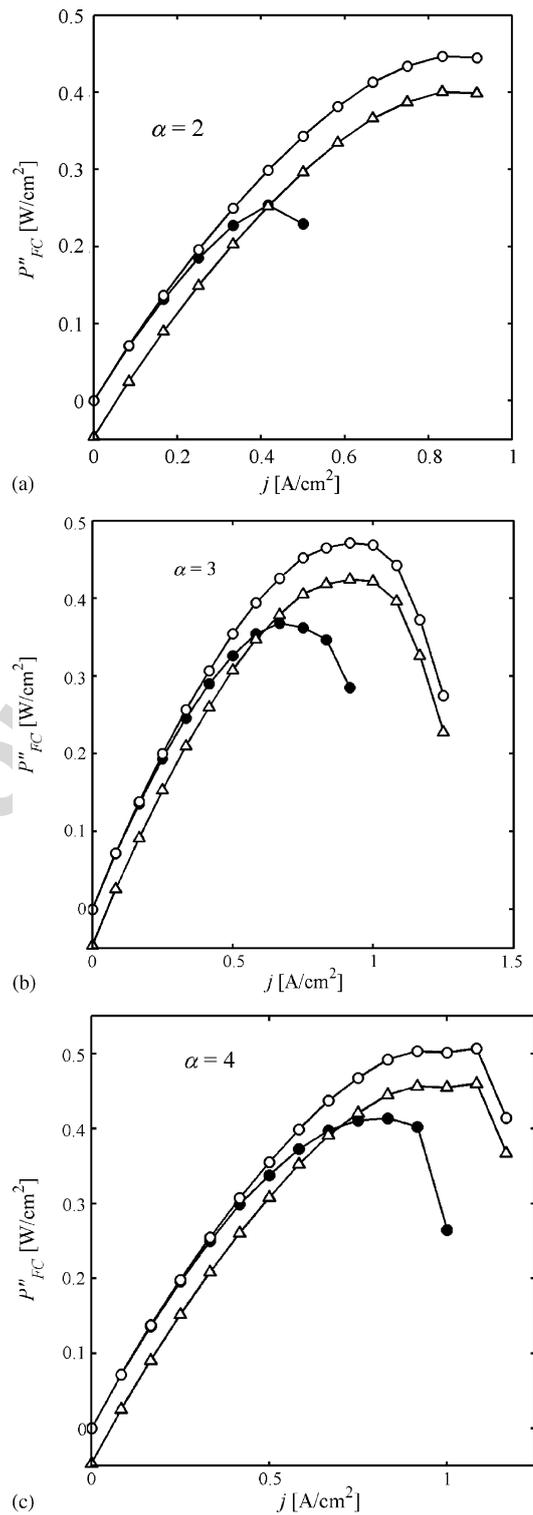

Fig. 7. Power density curves at $\alpha = 2$–4 with the EO pump on and off. Fig. 7a–c correspond to α of 2–4 respectively. The closed circles ($\bullet$) denote fuel cell power output with the EO pump deactivated, the open circles ($\bigcirc$) are the gross power density of the fuel cell with an activated EO pump, and the open triangles ($\triangle$) are net (fuel cell output power minus EO pump parasitic power) system power density with an activated EO pump. At low fuel cell current densities, there is no danger of flooding and the net fuel cell output power ($\bullet$) can, in this regime, be larger than the net fuel cell power with the EO pump activated ($\triangle$). For the $\alpha = 2$–4 cases, activation of the EO pump increases the net maximum power output of the cell by 57%, 18%, and 13%, respectively.

cell/pump system power output and significantly extends the operating range of the PEMFC.

4.3. Parasitic power loads of EO pumping

We have demonstrated that, for the conditions explored here, EO pumping power varies between about 50 and 65 mW (approximately 10% of the net power produced by the pump/cell system). In this section we revisit the simple EO pump power model presented earlier and apply it specifically to our design. First, as suggested earlier, we will use an empirical value of $V_{app} = 14$ V for our design. Second, for the present design, water is pumped in a direction with a component perpendicular to the field applied across the pump (see Fig. 3). We model this as an EO pump with a pumping area equal to the x–y cross-sectional area of the porous element. We then place a hydraulic load in series with this pump that includes a change in hydrostatic head and flow through a porous medium with the x–z cross-sectional area of the porous structure. This hydrostatic head is determined by the $\Delta z = 3$ mm change in elevation from the GDL to (the bottom of) the water reservoir. We characterize the y-direction flow through the porous structure using a Darcy's Law formulation [52] with the following permeability, κ:

$$\kappa = \frac{\psi a^2}{8\tau}. \tag{9}$$

Water conductivity is another critical parameter in the power ratio estimate. As discussed by Zeng et al. [54], typically the pH of water exposed to atmospheric conditions quickly reaches about 5.5 (e.g., measured 5 min after its production). Assuming this pH value is due solely to CO_2 adsorption and subsequent production of carbonic acid ions, the conductivity would be $3 \, \mu S \, cm^{-1}$. However, in practice we find the conductivity of water produced by the fuel cell is typically much larger than this. Direct measurements of the water produced by our cell after 45 min of operation reveal a conductivity of $170 \, \mu S \, cm^{-1}$. One possible explanation for this is iron contamination due to the presence of stainless steel in the current collectors [65]. Pozio et al. [66] have shown that Nafion degradation resulting from iron contamination can increase cathode effluent conductivity to nearly $200 \, \mu S \, cm^{-1}$. We are currently exploring ways to reduce this water conductivity due to contamination, including the removal of stainless steel current collectors, careful washing of materials, and system assembly in a clean environment [65].

Using the parameter estimates presented above, Eq. (7) predicts parasitic pump powers of roughly 80 mW (~13% of net system power) with 14 V applied potential for our single channel PEMFC. This is comparable to the actual 50–65 mW (~10% of net system power) observed in our systems [65].

5. Electrochemical impedance spectroscopy

Fuel cells are electrochemical systems often modeled as a network of linear and nonlinear electronic elements including resistors, capacitors, and complex impedance [67,68]. Spectroscopic impedance measurements can be obtained by imposing a low-magnitude AC perturbation on the steady performance of
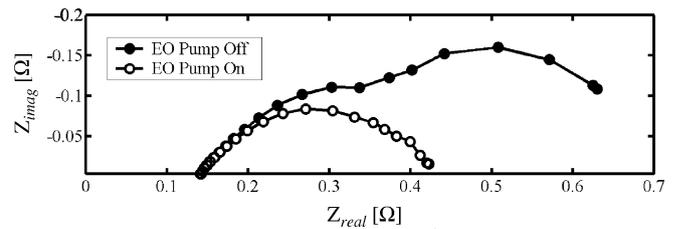

Fig. 8. Electrochemical impedance spectroscopy (EIS) measurements of the fuel cell with activated (○) and detactivated (●) EO pump. In both cases the cell potential is 0.8 V and measurement frequency ranges from 10 kHz to 0.1 Hz. The fuel cell was operated at a constant current density of 1 A cm^{-2} for 30 min prior to the start of these EIS experiments. The second loop in the EIS data for the deactivated EO pump case is strong indication that the fuel cell suffers from mass transfer losses without active pumping.

the fuel cell. Such measurements shed insight on the character of losses within the system as well as the hydration state of the PEM. In this section we present and briefly discuss preliminary electrochemical impedance spectroscopy (EIS) measurements we have performed on our combined PEMFC/EO pump system. Fig. 8 shows Nyquist plots of fuel cell impedance obtained at a constant cell potential of 0.8 V. Frequency here was varied from 10 kHz to 0.1 Hz and both curves were obtained after a 30 min run time. The plot shows the cases for the active EO pump (open symbols) and the inactive EO pump (closed symbols).

Under ideal (e.g., un-flooded) conditions, we model the fuel cell as a resistor in series with a parallel RC circuit [67]. The leftmost intercept on the x-axis corresponds to the high-frequency-limit, ohmic losses associated with contact resistance and electrolyte conductivity. The capacitive component of impedance is dominated by the effect of charged double layers at the cathode. The real component of the impedance in the parallel RC circuit is dominated by PEM conductance and reaction kinetics at the cathode. Double layer interactions and reaction kinetics at the anode of hydrogen PEMFC are typically negligible [8]. For this ideal case, we expect the Nyquist plot to be a simple semi-circle as we observe here for the activated EO pump case.

In contrast to the near-ideal performance with the EO pump activated, we note the Nyquist plot for the inactivated EO pump cases. At high frequency, the EIS measurements of both cases agree, showing that both cases have a well-hydrated PEM. However, we see a marked difference in performance at low frequencies. For the EO inactive case, the fuel cell cathode suffers significantly from mass transfer limitations due to cathode flooding. This flooding introduces additional impedance to the PEMFC, which is most apparent in the low frequency Nyquist plot. The additional mass transfer limitation in the gas diffusion layer results in the second "loop" in the Nyquist plot [18,31,68,69]. Though only a preliminary effort, this EIS measurement further supports that the EO pump improves fuel cell performance by mitigating mass transport limitations caused by liquid water in the cathode.

6. Conclusion

We have designed and tested a single channel PEMFC with integrated EO pumps for water removal. Galvanostatic, polar-

ization, and electrochemical impedance measurements demonstrate that EO pumping is a viable method of cathode water management. Electrochemical impedance tests suggest that EO pumps improve fuel cell performance by mitigating mass transfer limitations in fuel cell cathodes. Galvanostatic measurements show that EO pumps can be used to prevent cathode flooding, and enhance the performance of partially flooded PEMFCs. Polarization curves indicate that EO pumps are most beneficial in operating regimes prone to flooding, i.e. lower stoichiometric ratios and higher current densities. Power density curves show a net increase in maximum PEMFC system power density and current density upon activation of the electroosmotic pumps. The gain in maximum net power density is as high as 57% for the $\alpha = 2$ case.

Adequate water management is critical to robust and efficient fuel cell performance. Removal of liquid water with a low power, robust, active method should allow PEMFCs to operate in regimes otherwise inaccessible due to flooding, such as lower temperatures and high relative humidity. Water management can also reduce parasitic loads associated with air pumping by enabling operation at low stoichiometric ratios.

Acknowledgement

References

[1] G.Q. Lu, C.Y. Wang, T.J. Yen, X. Zhang, Electrochim. Acta 49 (2004) 821–828.
[2] J.S. Wainright, R.F. Savinell, C.C. Liu, M. Litt, Electrochim. Acta 48 (2003) 2869–2877.
[3] K. Tuber, M. Zobel, H. Schmidt, C. Hebling, J. Power Sources 122 (2003) 1–8.
[4] T.E. Springer, M.S. Wilson, S. Gottesfeld, J. Electrochem. Soc. 140 (1993) 3513–3526.
[5] D.P. Wilkinson, H.H. Voss, K. Prater, J. Power Sources 49 (1994) 117–127.
[6] R. Mosdale, S. Srinivasan, Electrochim. Acta 40 (1995) 413–421.
[7] T.E. Springer, T.A. Zawodzinski, S. Gottesfeld, J. Electrochem. Soc. 138 (1991) 2334–2342.
[8] D.M. Bernardi, M.W. Verbrugge, J. Electrochem. Soc. 139 (1992) 2477–2491.
[9] U. Pasaogullari, C.Y. Wang, J. Electrochem. Soc. 152 (2005) A380–A390.
[10] Z.H. Wang, C.Y. Wang, K.S. Chen, J. Power Sources 94 (2001) 40–50.
[11] K. Tuber, D. Pocza, C. Hebling, J. Power Sources 124 (2003) 403–414.
[12] S.H. Ge, X.G. Li, I.M. Hsing, Electrochim. Acta 50 (2005) 1909–1916.
[13] M.M. Mench, Q.L. Dong, C.Y. Wang, J. Power Sources 124 (2003) 90–98.
[14] F. Barbir, H. Gorgun, X. Wang, J. Power Sources 141 (2005) 96–101.
[15] F. Meier, G. Eigenberger, Electrochim. Acta 49 (2004) 1731–1742.
[16] R. Satija, D.L. Jacobson, M. Arif, S.A. Werner, J. Power Sources 129 (2004) 238–245.
[17] X.M. Ren, S. Gottesfeld, J. Electrochem. Soc. 148 (2001) A87–A93.
[18] T.E. Springer, T.A. Zawodzinski, M.S. Wilson, S. Gottesfeld, J. Electrochem. Soc. 143 (1996) 587–599.
[19] T.V. Nguyen, R.E. White, J. Electrochem. Soc. 140 (1993) 2178–2186.
[20] M. Watanabe, H. Uchida, Y. Seki, M. Emori, P. Stonehart, J. Electrochem. Soc. 143 (1996) 3847–3852.
[21] D. Natarajan, T. Van Nguyen, J. Power Sources 115 (2003) 66–80.
[22] R. Eckl, W. Zehtner, C. Leu, U. Wagner, J. Power Sources 138 (2004) 137–144.
[23] U. Pasaogullari, C.Y. Wang, J. Electrochem. Soc. 151 (2004) A399–A406.
[24] T.F. Fuller, J. Newman, J. Electrochem. Soc. 140 (1993) 1218–1225.
[25] T.A. Zawodzinski, M. Neeman, L.O. Sillerud, S. Gottesfeld, J. Phys. Chem. 95 (1991) 6040–6044.
[26] J.J. Baschuk, X.H. Li, J. Power Sources 86 (2000) 181–196.
[27] W.S. He, G.Y. Lin, T. Van Nguyen, AIChE J. 49 (2003) 3221–3228.
[28] J. Ihonen, M. Mikkola, G. Lindbergh, J. Electrochem. Soc. 151 (2004) A1152–A1161.
[29] G.Y. Lin, W.S. He, T. Van Nguyen, J. Electrochem. Soc. 151 (2004) A1999–A2006.
[30] N. Pekula, K. Heller, P.A. Chuang, A. Turhan, M.M. Mench, J.S. Brenizer, K. Unlu, Nucl. Instrum. Methods Phys. Res., Sect. A 542 (2005) 134–141.
[31] D.J.L. Brett, S. Atkins, N.P. Brandon, V. Vesovic, A. Vasileiadis, A. Kucernak, Electrochem. Solid-State Lett. 6 (2003) A63–A66.
[32] F.L. Chen, H.S. Chu, C.Y. Soong, W.M. Yan, J. Power Sources 140 (2005) 243–249.
[33] D. Hyun, J. Kim, J. Power Sources 126 (2004) 98–103.
[34] M.W. Knobbe, W. He, P.Y. Chong, T.V. Nguyen, J. Power Sources 138 (2004) 94–100.
[35] H.H. Voss, D.P. Wilkinson, P.G. Pickup, M.C. Johnson, V. Basura, Electrochim. Acta 40 (1995) 321–328.
[36] T. Van Nguyen, M.W. Knobbe, J. Power Sources 114 (2003) 70–79.
[37] E. Antolini, R.R. Passos, E.A. Ticianelli, J. Appl. Electrochem. 32 (2002) 383–388.
[38] B. Thoben, A. Siebke, J. New Mater. Electrochem. Syst. 7 (2004) 13–20.
[39] C. Lim, C.Y. Wang, Electrochim. Acta 49 (2004) 4149–4156.
[40] H.S. Chu, C. Yeh, F. Chen, J. Power Sources 123 (2003) 1–9.
[41] S. Litster, G. Mclean, J. Power Sources 130 (2004) 61–76.
[42] G.G. Park, Y.J. Sohn, T.H. Yang, Y.G. Yoon, W.Y. Lee, C.S. Kim, J. Power Sources 131 (2004) 182–187.
[43] Z.G. Qi, A. Kaufman, J. Power Sources 109 (2002) 38–46.
[44] M. Watanabe, M. Tomikawa, S. Motoo, J. Electroanal. Chem. Interfacial Electrochem. 182 (1985) 193–196.
[45] U. Pasaogullari, C.Y. Wang, Electrochim. Acta 49 (2004) 4359–4369.
[46] A.Z. Weber, J. Newman, J. Electrochem. Soc. 152 (2005) A677–A688.
[47] J. Chen, T. Matsuura, M. Hori, J. Power Sources 131 (2004) 155–161.
[48] S.H. Ge, X.G. Li, I.M. Hsing, J. Electrochem. Soc. 151 (2004) B523–B528.
[49] J.S. Yi, J.D.L. Yang, C. King, AIChE J. 50 (2004) 2594–2603.
[50] R.F. Probstein, Physicochemical Hydrodynamics, 2nd ed., John Wiley & Sons, Hoboken, NJ, 2003.
[51] N.A. Lacher, K.E. Garrison, R.S. Martin, S.M. Lunte, Electrophoresis 22 (2001) 2526–2536.
[52] S.H. Yao, J.G. Santiago, J. Colloid Interface Sci. 268 (2003) 133–142.
[53] D.J. Laser, J.G. Santiago, J. Micromech. Microeng. 14 (2004) R35–R64.
[54] S.L. Zeng, C.H. Chen, J.C. Mikkelsen, J.G. Santiago, Sens. Actuators, B 79 (2001) 107–114.
[55] P.H. Paul, D.J. Rakestraw, U.S. Patent 6,019,882, 2000.
[56] S.H. Yao, D.E. Hertzog, S.L. Zeng, J.C. Mikkelsen, J.G. Santiago, J. Colloid Interface Sci. 268 (2003) 143–153.
[57] J.A. Tripp, F. Svec, J.M.J. Frechet, S.L. Zeng, J.C. Mikkelsen, J.G. Santiago, Sens. Actuators, B 99 (2004) 66–73.
[58] S.H. Yao, A.M. Myers, J.D. Posner, K.A. Rose, J.G. Santiago, Submitted to J. MEMS, (2005).
[59] C.H. Chen, J.G. Santiago, J. MEMS 11 (2002) 672–683.
[60] D.J.L. Brett, S. Atkins, N.P. Brandon, V. Vesovic, N. Vasileiadis, A.R. Kucernak, Electrochem. Commun. 3 (2001) 628–632.
[61] Q. Dong, J. Kull, M.M. Mench, J. Power Sources 139 (2005) 106–114.
[62] A.A. Kulikovsky, H. Scharmann, K. Wippermann, Electrochem. Commun. 6 (2004) 729–736.
[63] J. Larminie, Fuel Cell Systems Explained, 2nd ed., John Wiley and Sons, San Francisco, 2003.
[64] A.A. Kulikovsky, Electrochim. Acta 49 (2004) 617–625.
[65] We have recently conducted experiments that support the hypothesis that iron-containing materials contribute to our water conductivity. We replaced

the stainless steel current collectors with gold plated aluminum. The conductivity of water produced in the cell cathode was reduced from $170\,\mu S\,cm^{-1}$ to less than $50\,\mu S\,cm^{-1}$. This lower conductivity corresponds to a parasitic EO pump power of 2 mW, roughly 4% of the maximum fuel cell power.

[66] A. Pozio, R.F. Silva, M. De Francesco, L. Giorgi, Electrochim. Acta 48 (2003) 1543–1549.

[67] R. O'hayre, S.W. Cha, W. Colella, F.B. Prinz, Fuel Cell Fundamentals, Wiley, 2005.

[68] V.A. Paganin, C.L.F. Oliveira, E.A. Ticianelli, T.E. Springer, E.R. Gonzalez, Electrochim. Acta 43 (1998) 3761–3766.

[69] M. Ciureanu, R. Roberge, J. Phys. Chem. B 105 (2001) 3531–3539.